Onset of fuzz formation in plasma-facing tungsten as a surface morphological instability

Chao-Shou Chen [1] Dwaipayan Dasgupta [2,*] Robert D. Kolasinski [3] Brian D. Wirth [2,4] and Dimitrios Maroudas [1,†]

[1] *Department of Chemical Engineering, University of Massachusetts, Amherst, Massachusetts 01003, USA*

[2] *Department of Nuclear Engineering, University of Tennessee, Knoxville, Tennessee 37996, USA*

[3] *Sandia National Laboratories, Livermore, California 94550, USA*

[4] *Fusion Energy Division, Oak Ridge National Laboratory, Oak Ridge, Tennessee 37830, USA*

(Received 16 July 2021; revised 24 September 2021; accepted 10 November 2021; published 24 November 2021)

Based on simulation results and theoretical analysis according to an atomistically informed continuum-scale model for the surface morphological response of tungsten plasma-facing component (PFC) in nuclear fusion devices, we demonstrate that the onset of the well-known surface nanostructure (known as "fuzz") formation in PFC tungsten is the outcome of a stress-induced surface morphological instability. Specifically, we show that formation and growth of nanotendrils emanating from the exposed surface of PFC tungsten, a precursor to fuzz formation, is caused by a long-wavelength surface morphological instability triggered by compressive stress in the PFC near-surface layer due to over-pressurized helium (He) bubbles forming in this near-surface region through implantation of low-energy He ions from the plasma. Using linear stability theory (LST), we predict the onset of surface growth in response to low-amplitude perturbations from a planar PFC surface morphology and calculate the average spacing between nanotendrils growing from the PFC surface, in excellent agreement with self-consistent dynamical simulations of surface morphological response according to the fully nonlinear surface evolution model starting with random fluctuations from the planar surface morphology that result in nanoscale surface roughness. In addition, we examine the morphological response of the PFC surface to low-amplitude perturbations of very long wavelengths from its planar morphology and interpret fully the simulation results on the basis of a weakly nonlinear tip-splitting instability theory, which predicts a post-instability nanotendril pattern formation with nanotendril separation consistent with the LST predictions regardless of the initial surface perturbation. Finally, we compare our simulation predictions for surface nanotendril growth with experimental measurements of fuzz layer growth on the exposed surface of PFC tungsten. Our simulation results are in very good agreement with the surface growth measurements at the early stages of fuzz growth, further establishing the onset of fuzz formation in PFC tungsten as the outcome of a stress-driven PFC surface morphological instability.

DOI: 10.1103/PhysRevMaterials.5.113403

I. INTRODUCTION

Tungsten is the chosen material for the divertor of nuclear fusion devices, a plasma-facing component (PFC) that is exposed to the extreme conditions of high heat and particle fluxes in the International Thermonuclear Experimental Reactor (ITER). The choice of tungsten as the PFC material for the ITER divertor is a result of its extraordinary thermomechanical properties including high melting point, high thermal conductivity, relatively low sputtering yield and low tritium retention, as well as low erosion [1–4]. However, under the typical operating conditions of He plasma exposure in ITER, the PFC surface temperature will be in the range of 900–2000 K and the He ion incident energy will be above a threshold of ∼35 eV, conditions consistent with the formation of the well-known fuzz surface nanostructure, a nanofiber-like structure, on the PFC tungsten surface [5–11]. The development of this fragile crystalline fuzz nanostructure severely changes the morphology of the He-exposed tungsten, and is responsible for adverse effects on the thermophysical properties of tungsten, such as its optical reflectivity, thermal conductivity, and mechanical strength [12–15].

Figure 1(a) gives a schematic representation of the evolution of a tungsten surface during He plasma irradiation, with nanotendrils growing from the surface as the He ion fluence increases and He bubbles form in the near-surface region and grow with continued exposure to the plasma. Nanotendrils emanating from the He-plasma-exposed tungsten surface have been shown to be the precursor to the formation of the fuzz surface nanostructure; such nanotendril formation is driven by stress-induced surface atomic diffusion with the stress originating from the over-pressurized helium bubbles that are trapped in the near-surface PFC tungsten region [16]. Due to the effects of subsurface bubble dynamics [17–20], He bubble bursting and crater formation on the surface [21–23], dislocation loop punching from large He bubbles [22,24,25], and many more mechanisms, these nanotendrils will continue to grow and subsequently evolve to the fuzz crystalline nanofiber-like structure, which is responsible for detrimental changes to the thermophysical properties of the He-implanted tungsten as a function of He content in the nanobubble region [14,26]. Many theoretical studies have focused on the

*ddasgupta@utk.edu

†maroudas@ecs.umass.edu

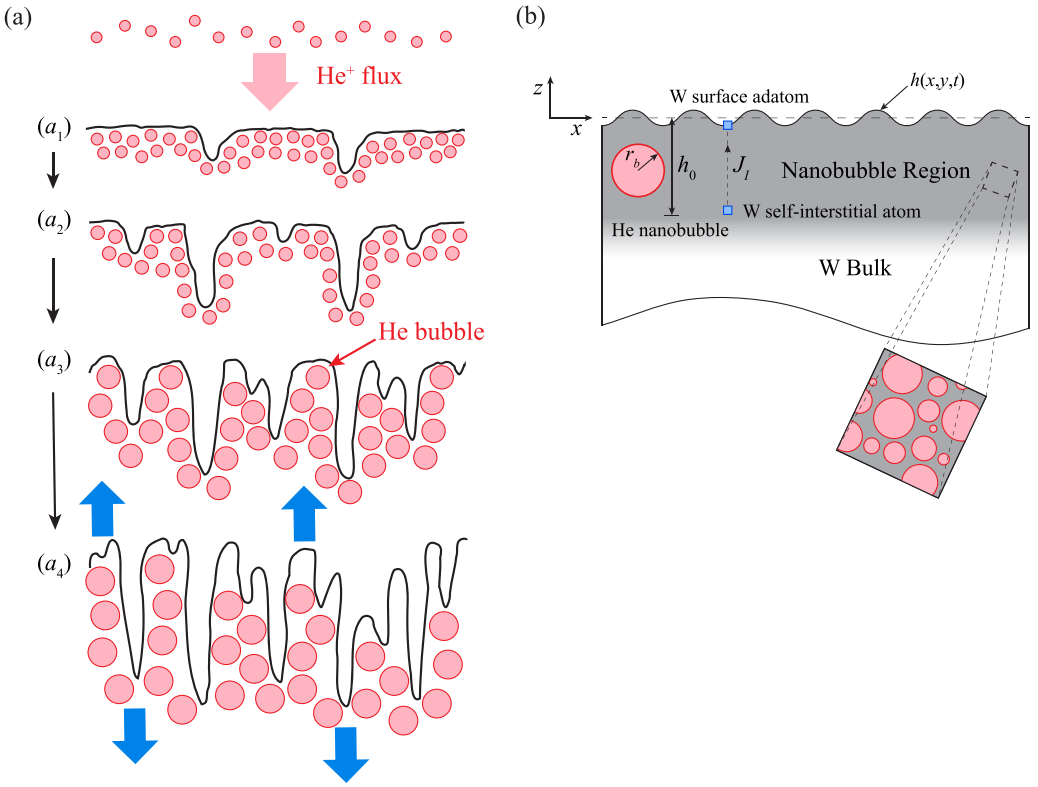

FIG. 1. Modeling of the onset of fuzz formation. (a) Schematic representation of the evolution of tungsten surface nanotendril growth (precursor to fuzz formation) during He plasma irradiation; the He ion fluence increases and the He bubbles formed in the near-surface region grow as time increases from (a_1) to (a_4). (b) Schematic representation of the homogenized near-surface nanobubble region of plasma-irradiated tungsten with W self-interstitial atoms migrating toward the exposed tungsten surface, at a flux J_I, and the surface being subjected to a long-wavelength perturbation from the planar morphology.

modeling of fuzz formation and growth and the prediction of the dependence of fuzz formation on temperature and incident He ion energy [27–35]. However, it is extremely challenging to capture the relevant length and time scales for fuzz growth on the PFC tungsten surface, on the order of micrometers and hours, through such a complex multiphysics process starting from atomic-scale concepts and simulations.

We have developed a 3D hierarchical continuum-scale model using atomistically derived constitutive information to study the onset of fuzz formation in PFC tungsten [16,36–38]. According to our model, stress-induced surface diffusion drives the morphological response of the He plasma-irradiated tungsten surface, where the stress in the near-surface region of PFC tungsten originates from the trapped over-pressurized He bubbles that form in this region due to the He plasma exposure. The migration to the tungsten surface of the W self-interstitial atoms ejected by the helium clusters and bubbles in the nanobubble region is another driver of surface morphological evolution. In the model, we assume the nanobubble region under the surface of PFC tungsten to be a thin homogenized layer of 30 nm in thickness, consistent with experimental findings [39], with uniform number density of nanobubbles; the bulk tungsten crystal below the nanobubble layer is modeled as a semi-infinite rigid medium. In previous studies, we validated the model predictions for the PFC surface morphology and the onset of fuzz formation and demonstrated that the average bubble size at He saturation and the steady-state He content in the nanobubble region have strong effects on the growth rate of the nanotendrils emanating from the surface of PFC tungsten [16]. In addition, we studied the effect of surface temperature on the growth rate of nanotendrils emanating from the plasma-exposed tungsten surface, showed that increasing temperature accelerates the growth of nanostructures, and demonstrated the importance of the plasma exposure duration in determining the surface morphological response [36]. We also explored the effect of softening of the tungsten elastic properties in the nanobubble region during He plasma exposure [26,40] and showed that it accelerates the growth of nanotendrils from the PFC tungsten surface [37]. Moreover, we accounted for the He bubble bursting and crater formation introducing nanometer-scale holes onto the PFC tungsten surface at prescribed rates and areal densities and demonstrated that this hole formation effect further accelerates the growth of nanotendrils and introduces fine-scale nanotendrils into the surface with an average spacing between such fine nanotendrils that is consistent with experimental measurements [16,38].

In stressed elastic solids, surface morphological instabilities may be triggered by stress winning the competition between elastic strain energy and surface energy, such as in the Asaro-Tiller or Grinfeld (ATG) instability [41,42], which has been widely studied both experimentally [43–46] and theoretically [47–52]. Such morphological instability analyses can offer important insights into surface nanostructure formation

in complex material systems, such as PFC tungsten. The purpose of this article is to establish the onset of fuzz formation in PFC tungsten as such a stress-induced surface morphological instability phenomenon. Using the 3D continuum-scale model outlined above and self-consistent dynamical simulations of PFC surface morphological response, we demonstrate that a PFC tungsten surface perturbed from its planar morphology after the He content in the near-surface region reaches steady state evolves to form a pattern of nanotendrils that emanate from the surface and grow fast to reach heights of tens of nanometers at over an hour of plasma exposure and average separation on the order of 1 μm. Such nanotendril separations are consistent with experimentally observed coarse surface features on PFC tungsten surfaces and are explained fully by linear stability theory. In addition, the independence of the key features of the nanotendril pattern from the wavelength of the initial perturbation is demonstrated, even at very long wavelengths, by a weakly nonlinear tip-splitting instability theory. Perhaps more importantly, our modeling predictions for the surface growth rate are in agreement with our experimental measurements of fuzz layer growth at the early stages of fuzz nanostructure formation.

II. MODEL, SIMULATION TECHNIQUES, AND EXPERIMENTAL METHODS

A. PFC tungsten surface evolution model

In our model of PFC tungsten surface morphological response, we consider a homogenized continuous nanobubble layer in the PFC near-surface region of average thickness h_0 and nanobubble radius r_b with a uniform number density of He bubbles depicted schematically in Fig. 1(b) as the uniformly gray-shaded upper region of the PFC material domain. The incident energy of He ions considered in this study is below the sputtering threshold (∼100 eV), leading to a negligible sputtering loss of tungsten atoms [16,20]. Ignoring such sputtering losses, the governing equation for the morphological evolution of the helium-plasma-irradiated tungsten surface that guarantees conservation of tungsten atoms has been reported in our previous work [16] and is given by

$$\frac{\partial h}{\partial t} = H'\Omega\nabla_s \cdot \mathbf{J}_s + \Omega J_{\mathrm{I}}, \tag{1}$$

where $h = h(x, y, t)$ is the surface height function with x, y, and z being the usual Cartesian coordinates, $H' \equiv [1 + (\frac{\partial h}{\partial x})^2 + (\frac{\partial h}{\partial y})^2]^{1/2}$, ∇_s is the surface gradient operator, Ω is the atomic volume of tungsten at temperature T, $\mathbf{J}_s$ is the atomic surface mass flux, and J_{I} is the self-interstitial flux from the bulk of the nanobubble region to the plasma-exposed surface along the z direction. In the model, dislocation loop formation and the process of loop punching from helium bubbles in the near-surface nanobubble region are approximated as a flux of self-interstitial atoms (SIAs) to the surface. The surface flux, $\mathbf{J}_s = \frac{D_s\delta_s}{k_B T}\nabla_s(\mu/\Omega)$, is proportional to the surface gradient of the chemical potential, μ, of surface atoms, where k_B is the Boltzmann constant, δ_s/Ω is the number of surface atoms per unit area, and D_s is the surface atomic diffusivity that is an Arrhenius function of temperature [53]. The SIA flux, $J_{\mathrm{I}} = -\frac{D_{\mathrm{I}}C_{\mathrm{I}}}{k_{\mathrm{B}}T}\nabla_z\mu_{\mathrm{I}}$, is proportional to the gradient of the chemical potential of tungsten SIAs, μ_{I}, along the z direction [see Fig. 1(b)], where D_{I} is the SIA diffusivity at temperature T and C_{I} is the homogenized SIA concentration in the nanobubble region [54]. The chemical potential of the surface atoms, μ, is determined by the curved surface free energy and the elastic strain energy at the surface, with a biaxial compressive stress induced in the near-surface region due to the formation of over-pressurized helium bubbles by the implanted helium [16]. The competition between elastic strain energy (that drives surface growth through formation of nanotendrils emanating from the surface) and surface free energy (that drives surface smoothening) leads to surface morphological change and triggers a surface morphological instability; the linearized model for the surface morphological response of PFC tungsten, including a full description of the chemical potential of surface atoms and an asymptotic calculation of the elastic strain energy density in the near-surface region of PFC tungsten, is derived in the Supplemental Material document [55]. The pressure of the He bubbles in the PFC nanobubble region is determined by the equation of state for helium [56], with the parametrization of the He bubble density obtained by analysis of large-scale molecular-dynamics (MD) simulation results [18,57]. In this study, helium bubbles in the PFC nanobubble region are assumed to be spherical, with the He/W interfacial free energy at the bubble/matrix interface taken to be isotropic.

To examine the morphological stability of the plasma-exposed tungsten surface with a planar surface morphology, we performed dynamical simulations of surface morphological evolution starting from a nanobubble region configuration, where the He concentration has reached steady state and subjecting the surface to a low-amplitude perturbation from the planar morphology [see Fig. 1(b)]. After the He content in the near-surface region of PFC tungsten reaches steady state, the actual flux of retained helium in the near-surface region balances the flux of released He due to bubble bursting, so that the He concentration in this nanobubble region is maintained at steady state. At this state, the implanted He will form new bubbles through so-called trap-mutation reactions which also generate W SIAs in the nanobubble region; the trap-mutation process generates Frenkel pairs (vacancy-SIA pairs) with the vacancies forming the helium-vacancy complexes that constitute the He nanobubbles and the SIAs being injected into the W matrix in the vicinity of the bubbles. Consequently, the homogenized SIA concentration, $C_{\mathrm{I}}(t)$, at a time instant t is expressed as

$$C_{\mathrm{I}}(t) = \frac{\dot{r}_{\mathrm{burst}}\left(\frac{(4/3)\pi r_{b,s}^3}{\Omega}\right)A\,t - F_{\mathrm{I}}}{V}, \tag{2}$$

where $r_{b,s}$ is the nanobubble radius at steady state for the He content in the PFC nanobubble region (which is also equal to the average radius of the bursting bubbles), A is the area of the exposed tungsten surface, V is the volume of the nanobubble region, and $\dot{r}_{\mathrm{burst}}$ is the He bubble bursting rate; this rate of bubble bursting is taken to be consistent with experimental measurements and was validated in our previous study [38]. F_{I} is the total number of SIAs that migrate to the PFC tungsten surface up to time t, with t measured from when the He content in the near-surface region reaches steady state, and

is given by

$$F_{\mathrm{I}}(t) = \int_0^t \int_0^A J_{\mathrm{I}}\, dA\, dt. \tag{3}$$

The initial condition for the SIA concentration, $C_{\mathrm{I},0}$, is obtained by equating at steady state the volumetric rate of generation of W SIAs from trap-mutation reactions with the rate of loss of SIAs due to the self-interstitial mass flux to the PFC surface, which (for a planar surface morphology) gives

$$C_{\mathrm{I},0} = \dot{r}_{\mathrm{burst}} \left(\frac{(4/3)\pi r_{b,s}^3 h_0}{D_{\mathrm{I}}\Omega} \right) \times \left(\frac{k_{\mathrm{B}}T}{E_{\mathrm{I}}^f + \sigma_{0,s}(\Omega_r - \Omega) - \Omega\mathcal{E}_{0,s}} \right). \tag{4}$$

In Eq. (4), h_0 is the average thickness of the nanobubble region, E_{I}^f is the formation energy of SIAs [16], $\sigma_{0,s}$ is the average stress level in the near-surface nanobubble region at steady state for the He concentration, Ω_r is the relaxation volume of the SIA [40], and $\mathcal{E}_{0,s}$ is the leading order of the elastic strain energy density at steady state for the He content [55]; this leading-order term corresponds to a planar PFC surface morphology.

In this study, the average bubble size and the He content at steady state are chosen as $r_{b,s} = 1$ nm and $n_{\mathrm{He},s} = 16\%$, respectively, which are consistent with experimental findings in the literature [10,39]. We have examined and validated the effect of varying $r_{b,s}$ and $n_{\mathrm{He},s}$ in our previous work [16,36,37]. The temperature is set at $T = 1100$ K, which is within the temperature range expected in the divertor region [9]; the effect of temperature on the PFC tungsten surface morphological response has been explored in our previous study [36]. Finally, the elastic moduli of tungsten in the He-irradiated nanobubble region are calculated using exponential scaling relations for the moduli dependence on the He concentration properly parameterized by analysis of MD simulation results [26] that account for the irradiation-induced elastic softening of the PFC near-surface region. A more detailed description of the model and its parametrization can be found in Refs. [16,36–38].

B. Numerical simulations

We performed dynamical simulations of surface morphological evolution of the He plasma-exposed tungsten, employing tungsten supercells with lateral dimensions over the range from 10 μm × 10 μm to 20 μm × 20 μm with the surface discretized by using a $N \times N$ grid. We applied periodic boundary conditions in the lateral directions, and set the average thickness of the nanobubble region to $h_0 =$ 30 nm, which is consistent with experimental findings [39]. The discretized surface height $h(i, j, t)$ represents the surface morphology obtained from the morphological evolution simulations with the local surface height function, h, evaluated at each surface grid point (i, j), where $i, j \in \{1, 2, \ldots, N\}$ at a time instant t. To solve the elastostatic boundary-value problem (BVP), we implemented a spectral collocation method and discrete fast Fourier transforms (FFTs) to compute the stress field in the nanobubble layer. The elastostatic BVP is coupled self-consistently with the evolution of the surface morphology, which is monitored by applying an operator-splitting semi-implicit front tracking method with adaptive time step size [16,47,58,59].

To guarantee the accuracy of the simulation predictions while maintaining a reasonable computational cost, we performed systematic convergence tests for the computed morphological metrics (such as RMS surface roughness) with the surface grid size. We found that $N = 1024$ generated a sufficiently fine grid resolution for numerical calculation purposes; numerical accuracy with such a surface grid resolution was validated in our recent simulation study [38]. With the above numerical implementation of our surface morphological evolution model for PFC tungsten, we considered a W(110) surface with an initially nano-scale rough surface and performed our simulations using initial surface configurations with RMS surface roughness $SR(t = 0) = 5$ nm at steady state for the He content, where we either perturbed the surface randomly, with a low-amplitude perturbation corresponding to thermal fluctuations from a planar surface morphology, or subjected the planar surface to a low-amplitude plane-wave perturbation with perturbation wavelength ranging from 3.33 μm to 20 μm. The need for such simulations of surface morphological response to low-amplitude, long-wavelength perturbations is explained and discussed in Sec. III. The initial nanoscale surface roughness of W used in this study is consistent with the initial RMS surface roughness of ITER-grade W samples properly prepared for plasma exposure experiments and characterization of the resulting plasma-exposed surfaces, as reported in Ref. [16] and in this study.

C. Experiments

For comparison with the theoretical results presented in this study, we have conducted experimental characterization of the surface morphology of polycrystalline tungsten specimens that were exposed to high-flux helium plasmas. The details of these plasma exposures are included in our prior work (cf. Ref. [16]), and only a short summary is provided here. A series of five polycrystalline "ITER-grade" tungsten specimens were machined into 7.6 mm diameter discs and mechanically polished to a mirror finish, with RMS surface roughness less than 10 nm. Following surface preparation, we annealed the samples to a temperature of 1000 °C in vacuum for 1 hr at a base pressure lower than 10^{-6} Torr. The specimens were then secured to a button-style resistive heater and inserted into an RF plasma source equipped with a Lisitano coil. Each sample analyzed here was heated to 840 ± 15 °C prior to the start of each experiment. Once a discharge was initiated, we monitored the incident plasma flux intermittently using a Langmuir single probe [60]. For the exposures reported here, the incident plasma flux was $\Gamma_{\mathrm{ion}} = 2.7 \times 10^{20}$ m^{-2} s^{-1}. We adjusted the incident ion energy to 75 eV by applying a negative bias to the specimen. Plasma fluences over the range 5.0×10^{23}–1.2×10^{25} m^{-2} were achieved by varying the exposure time between 30 min. and 6 hrs.

For surface morphologies that formed at low helium fluence, we used atomic force microscopy (AFM) to measure RMS variations in surface height (see Ref. [16] for further details.) In cases where the surface morphology was in a more advanced state of growth (i.e., where distinct nanotendrils

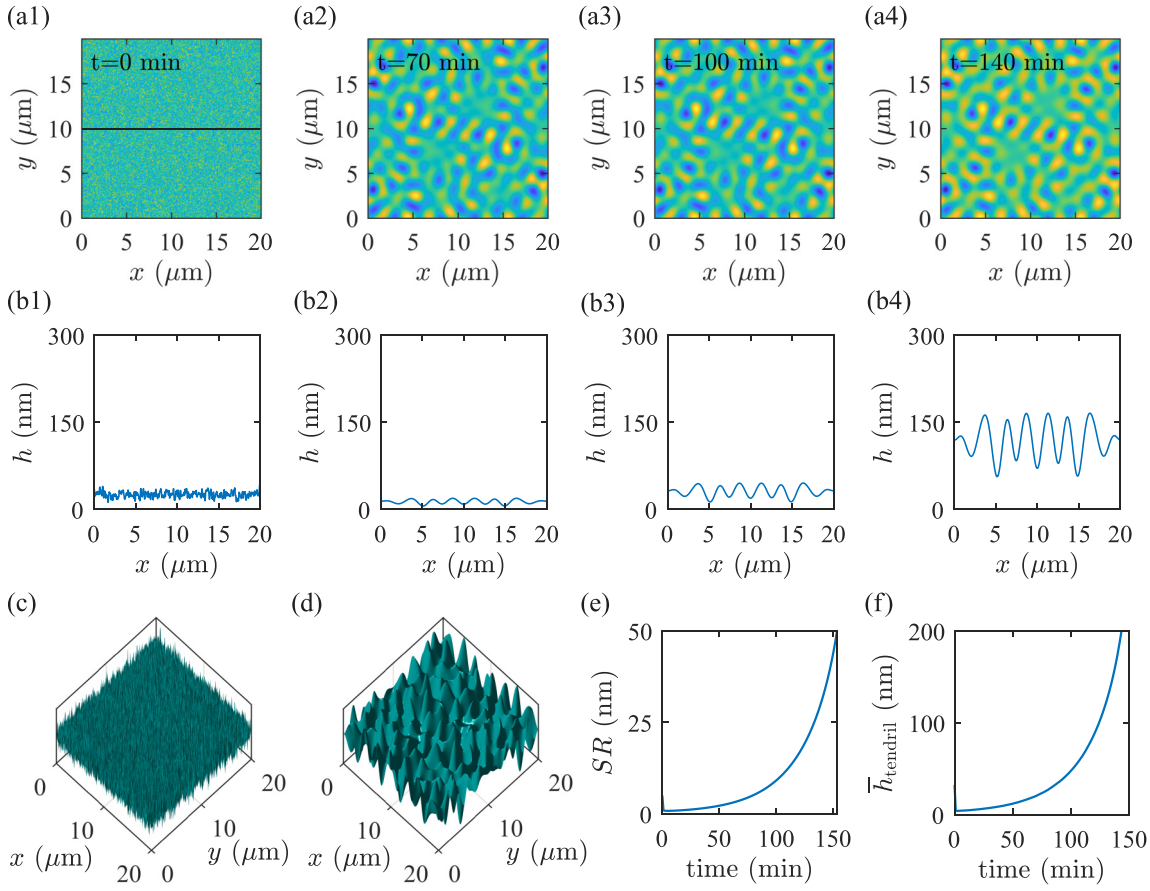

FIG. 2. Morphological evolution of a W(110) surface starting with a random low-amplitude perturbation from a planar morphology at an initial nanoscale surface roughness $SR = 5$ nm, with the surface being exposed to a 75 eV He plasma irradiation with a He flux of 2.7×10^{20} ions m^{-2} s^{-1} at $n_{\mathrm{He},s} = 16\%$, $r_{b,s} = 1$ nm, $T = 1100$ K, and $\dot{r}_{\mathrm{burst}} = 2.67 \times 10^{12}$ m^{-2} s^{-1}. [(a1)–(a4)] Top views of the tungsten surface morphology in the form of contour maps of the surface height function $h(x, y, t)$ at (a1) $t = 0$, (a2) 70, (a3) 100, and (a4) 140 min after initiation of plasma exposure. [(b1)–(b4)] Cross-sectional views of tungsten surface profiles along the black horizontal solid line marked in (a1) at the time instants corresponding to [(a1)–(a4)], respectively. [(c)-(d)] 3D views of the tungsten surface morphology corresponding to the top views shown (c) in (a1) and (d) in (a4). Evolution of (e) RMS surface roughness $SR(t)$ and (f) average nanotendril height, $\bar{h}_{\mathrm{tendril}}(t)$.

begin to emerge from the surface), use of the AFM is not effective. In these situations, we imaged specimens using a Zeiss ORION NanoFab helium ion microscope (HIM) to assess any changes in surface morphology. The main approach to determining the thickness of helium-induced nanostructure layer was through focused ion beam (FIB) profiling using a 25 keV Ga^+ ion beam. The tungsten nanostructure is delicate, and as a result, a low current beam (<10 pA) was used for the FIB profiling to ensure that a clean cut could be produced. After cutting a 3-μm-wide profile into the material, we imaged each cross section using HIM at an angle of 54° referenced with respect to the surface normal. The HIM images were acquired using a 1 pA, 25 keV He^+ beam. The surface height variation was then measured directly from the HIM images, correcting for the 54° tilt angle. Additional details are presented in the Supplemental Material document [55].

III. RESULTS

A. Simulated surface morphological evolution

Figure 2 shows representative simulation results for the surface morphological response of PFC tungsten starting with a random low-amplitude perturbation from a planar PFC surface morphology at steady state for the He concentration along with a detailed characterization of the topographical features of the He-implanted tungsten surface. In the simulations, we have used typical He irradiation conditions, represented by the simulation parameters: He plasma incident energy of 75 eV with a He flux of 2.7×10^{20} ions m^{-2} s^{-1} at $n_{\mathrm{He},s} = 16\%$, $r_{b,s} = 1$ nm, $T = 1100$ K, and $\dot{r}_{\mathrm{burst}} = 2.67 \times 10^{12}$ m^{-2} s^{-1}. The top views of the simulated PFC tungsten surface morphology, with the corresponding times of plasma exposure noted, are shown in Figs. 2(a1)–2(a4), respectively. The corresponding cross-sectional views of the tungsten surface profiles along the black horizontal solid line marked in Fig. 2(a1) are shown in Figs. 2(b1)–2(b4). The 3D views of the initial PFC surface configuration and the tungsten surface morphology at $t = 140$ min of plasma exposure corresponding to Figs. 2(a1) and 2(a4) are shown in Figs. 2(c) and 2(d), respectively. The evolution of the two surface characterization metrics for the plasma-exposed tungsten surface, namely, the RMS surface roughness, $SR(t)$, and the average nanotendril height, $\bar{h}_{\mathrm{tendril}}(t)$, is shown in Figs. 2(e) and 2(f), respectively. In both cases, the evolution of the two surface characterization metrics

indicates that perturbing the planar PFC surface with the He concentration having reached steady state in the nanobubble region leads to an initial decrease in the surface roughness and average nanotendril height at the very early stage of evolution due to the dominance of the surface curvature gradient as a driver of surface evolution. However, this early evolution stage is extremely short, followed by a steady increase of both morphological metrics as a result of the induced stress level in the nanobubble region overcoming the surface curvature and becoming the dominant driving force for surface evolution.

It is clearly observed from the simulated surface morphologies at a He plasma-exposure time of 140 min after the planar PFC surface was perturbed, shown in Figs. 2(a4), 2(b4), and 2(d), that nanotendrils are emanating from the PFC tungsten surface with the simulated average nanotendril height being approximately 173 nm as shown in Fig. 2(f). In addition, the average spacing between neighboring nantendrils obtained from the simulation results is approximately 2–2.5 μm, which is consistent with the predicted maximally unstable wavelength, $\lambda_{\max}$, from a linear stability analysis as we will see in Sec. III B 1. The average nanotendril width can be estimated as approximately half of the average nanotendril spacing.

B. Surface morphological stability analysis

1. Linear stability theory

In order to provide a fundamental theoretical interpretation of the surface morphological response of PFC tungsten documented in the results of Fig. 2, we performed a linear stability analysis of the planar PFC surface morphological response to a low-amplitude plane-wave perturbation. For low-energy He exposure, the steady-state He content is reached within a few hundred seconds of exposure [39] and in that short transient period no significant morphological change is observed [16,39]. Therefore, without loss of generality, the morphological stability of a planar W surface under steady-state He content can be analyzed to understand the origin of formation of surface nanotendrils—a precursor to fuzz formation. To examine its morphological stability, the planar W surface is subjected to a low-amplitude plane-wave perturbation, $\Delta_0 \exp(i\mathbf{k}\cdot\mathbf{x})$ with wave vector $\mathbf{k} = (k_x, k_y)$ and $\Delta_0 k \ll 1$, and the elastic strain energy density $\mathcal{E}$ is calculated [47,59]. For linear stability analysis, $\mathcal{E}$ and the local surface curvature κ are approximated retaining up to the linear-order terms in the respective expansions according to the small-slope approximation, $\sqrt{h_\alpha h_\alpha} \ll 1$, where $\alpha = x$ or y and the use of repeated indices implies the summation convention.

Making the lengths and time dimensionless with a length scale $l \equiv M_0\gamma/\sigma_{0,s}^2$ and a time scale $\tau \equiv k_B T l^4/[D_s\Omega\delta_s\gamma]$, respectively, where $M_0 = E_0/(1-\nu_0^2)$ and γ are the biaxial modulus and surface free energy per unit area, respectively, of pure W at temperature T, writing Eq. (1) in dimensionless form, linearizing it, and using a trial solution of $\tilde{h}(x,y,t) = \tilde{h}_0 + \tilde{\Delta}_0 \exp(\tilde{\omega}\tilde{t})\exp(i\tilde{\mathbf{k}}\cdot\tilde{\mathbf{x}})$, in which tildes denote dimensionless quantities, results in the dimensionless dispersion relation

$$\tilde{\omega} = -\tilde{k}^4 + 2\tilde{k}^3 - \Xi_I\tilde{k}^2 + 2\Xi_I\tilde{k}. \tag{5}$$

In Eq. (5), $\tilde{\omega}$ is the real part of the characteristic dimensionless growth or decay rate of the perturbation from the planar surface morphology with dimensionless wave number $\tilde{k} \equiv \sqrt{\tilde{k_x}^2 + \tilde{k_y}^2}$, and $\Xi_I \equiv \frac{D_I C_{I,0}\Omega l^2}{D_s\delta_s h_0}$ is a dimensionless parameter that expresses the relative strength of the W self-interstitial atomic flux towards the free surface with respect to the surface diffusional mass flux. Using the values of the physical properties and other parameters reported in Ref. [16] and those parameters used to produce the results of Fig. 2, we obtain for l and τ the values of approximately 0.50 μm and 53.8 min, respectively. At steady-state helium concentration in the nanobubble region, the SIA mass flux does not play a significant role, yielding a value of $\Xi_I \approx \mathcal{O}(10^{-9})$, and $\tilde{\omega}$ is positive for $\tilde{k} \lessapprox 2$, which implies that any longer-wavelength perturbation from the planar surface morphology will grow over time and develop protrusions on the surface resulting in formation of nanotendrils; the maximally unstable wave number is $\tilde{k}_{\max} \approx 1.5$ and the corresponding wavelength is $\lambda_{\max} \approx 2.11$ μm. Therefore we conclude that the nanotendril growth on the He-plasma irradiated W surface is the outcome of a surface morphological instability, driven by the competition between the surface free energy and the stress in the nanobubble region that originates from the over-pressurized He bubbles formed by the implanted He. In our model, the SIA concentration at steady state of He content is dependent on the rate of bubble bursting, which is difficult to measure experimentally. Based on our estimate [38], this SIA concentration is low and, therefore, it practically plays no role in driving the PFC surface evolution; additionally, the results of the linear stability analysis will not change even if the actual SIA concentration is higher than the currently estimated value by a few orders of magnitude.

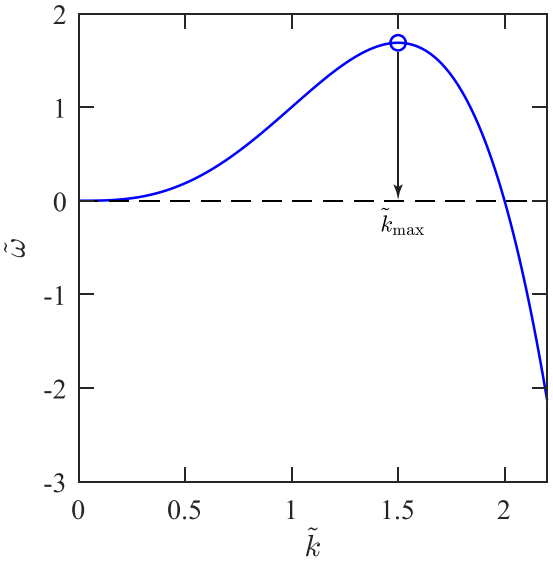

FIG. 3. Dimensionless dispersion relation $\tilde{\omega} = \tilde{\omega}(\tilde{k})$ for the real part of the surface perturbation growth rate as a function of perturbation wave number, where $\tilde{k} \equiv \sqrt{\tilde{k}_x^2 + \tilde{k}_y^2}$. The blue open circle and downwards pointing arrow are used to mark the maximally unstable wave number $\tilde{k}_{\max} \approx 1.50$.

Figure 3 shows the dependence of the real part of the dimensionless surface perturbation growth rate $\tilde{\omega}$ on the dimensionless perturbation wave number $\tilde{k}$ according to the dimensionless dispersion relation given in Eq. (5). The

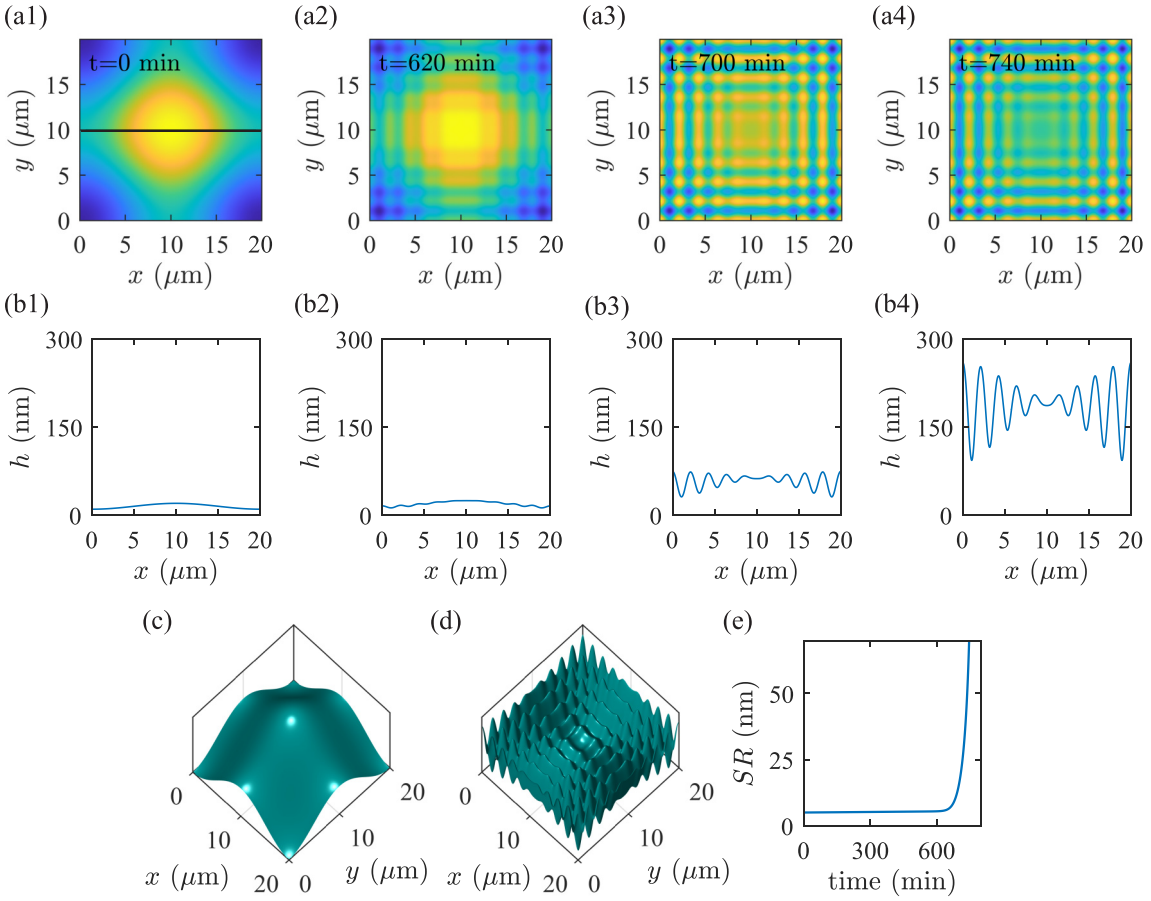

FIG. 4. Morphological evolution of a W(110) surface starting with a specific low-amplitude long-wavelength perturbation from a planar morphology, $h = h_0 + \Delta_0[\exp(i2\pi x/\lambda_p) + \exp(i2\pi y/\lambda_p)]$, under He incident ion energy and flux conditions identical to those in Fig. 2 at $n_{\mathrm{He},s} = 16\%$, $r_{b,s} = 1$ nm, $T = 1100$ K, and $\dot{r}_{\mathrm{burst}} = 2.67 \times 10^{12}$ m^{-2} s^{-1}, where the wavelength of the surface perturbation is $\lambda_p = 20\,\mu$m. [(a1)–(a4)] Top views of the tungsten surface morphology in the form of contour maps of the surface height function $h(x, y, t)$ at (a1) $t = 0$, (a2) 620, (a3) 700, and (a4) 740 min after initiation of plasma exposure. [(b1)–(b4)] Cross-sectional views of tungsten surface profiles along the black horizontal solid line marked in (a1) at the time instants corresponding to [(a1)–(a4)], respectively. [(c) and (d)] 3D views of the tungsten surface morphology corresponding to the top views shown (c) in (a1) and (d) in (a4). (e) Evolution of RMS surface roughness $SR(t)$.

result of the linear stability analysis gives a single maximally unstable wave number, $\tilde{k}_{\mathrm{max}} \approx 1.50$, marked in Fig. 3, which corresponds to the dimensionless maximally unstable wavelength $\tilde{\lambda}_{\mathrm{max}}$, and dominates the driven post-instability evolution from the perturbed planar surface morphology. Hence, the linear stability analysis implies that a surface morphological instability is triggered by perturbing the PFC planar surface with a dominant surface growth rate $\tilde{\omega}(\tilde{k}_{\mathrm{max}})$ that controls the growth rate of the nanotendrils that form on the surface of He-implanted tungsten, while the average separation between nanotendrils is determined by the maximally unstable wavelength $\tilde{\lambda}_{\mathrm{max}}$.

2. *Weakly nonlinear tip-splitting instability theory*

A major issue in the analysis of surface morphological response, governed by the surface morphological instability that was discussed in Sec. III B 1, arises by considering the response of the surface to low-amplitude but long-wavelength perturbations. In such a situation, the wavelength is much longer than the separation distances of the nanometer-scale surface features characteristic of the initial configuration of the PFC surface in Fig. 2(c), perturbed from the planar morphology, considered in the simulations of Fig. 2, or even wavelengths that are much longer than the maximally unstable wavelength predicted by the linear stability theory. Such long wavelengths may be excited in real samples of PFC tungsten and are particularly challenging to handle with the periodic supercells in our simulations. Therefore we examined the morphological response of the planar PFC tungsten surface to low-amplitude long-wavelength perturbations, and with wavelengths that are comparable to the dimensions of our computational supercells; such wavelengths are longer by three orders of magnitude compared to the surface features of the initial configuration of Fig. 2(c) characteristic of random nanometer-scale perturbations from the planar PFC surface morphology.

Figures 4 and 5 show simulation results for the surface morphological evolution of PFC tungsten starting with a specific low-amplitude perturbation from a planar surface morphology, with long-wavelength perturbations as described in the captions of Figs. 4 and 5, respectively, at steady-state He content together with a detailed characterization of the topographical features of the He-implanted tungsten surface

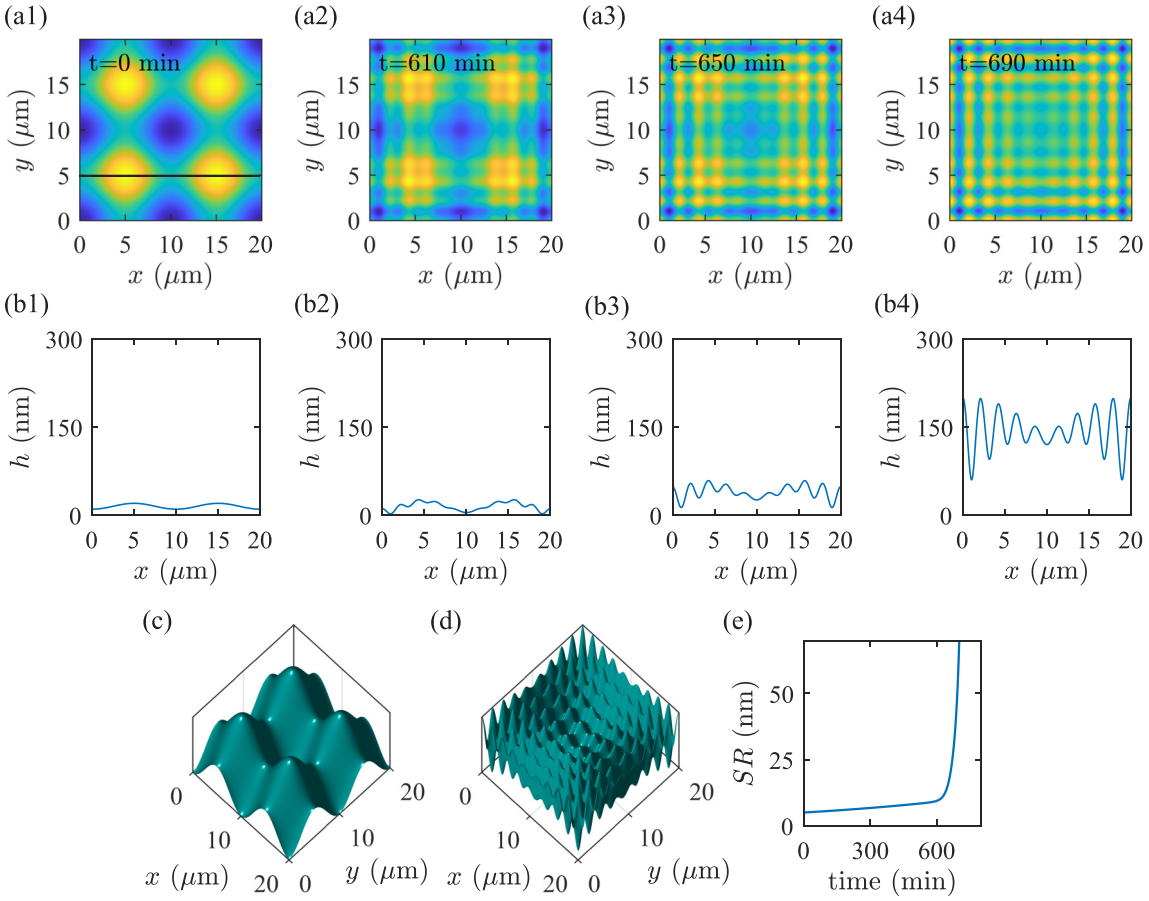

FIG. 5. Morphological evolution of a W(110) surface starting with a specific low-amplitude long-wavelength perturbation from a planar morphology, $h = h_0 + \Delta_0[\exp(i2\pi x/(\lambda_p)) + \exp(i2\pi y/(\lambda_p))]$, under He incident ion energy and flux conditions identical to those in Fig. 2 at $n_{\mathrm{He},s} = 16\%$, $r_{b,s} = 1$ nm, $T = 1100$ K, and $\dot{\imath}_{\mathrm{burst}} = 2.67 \times 10^{12}$ m^{-2} s^{-1}, where the wavelength of the surface perturbation is $\lambda_p = 10$ μm. [(a1)–(a4)] Top views of the tungsten surface morphology in the form of contour maps of the surface height function $h(x, y, t)$ at (a1) $t = 0$, (a2) 610, (a3) 650, and (a4) 690 min after initiation of plasma exposure. [(b1)–(b4)] Cross-sectional views of tungsten surface profiles along the black horizontal solid line marked in (a1) at the time instants corresponding to [(a1)–(a4)], respectively. [(c) and (d)] 3D views of the tungsten surface morphology corresponding to the top views shown (c) in (a1) and (d) in (a4). (e) Evolution of RMS surface roughness $SR(t)$.

under He irradiation conditions identical to those that yielded the results of Fig. 2. The imposed perturbation wavelengths in Figs. 4 and 5 are equal to the length of the supercell edge and one half of the supercell edge length (in the lateral directions of the supercell), respectively. The top views of the simulated PFC tungsten surface morphology are shown in Figs. 4(a1)–4(a4) and 5(a1)–5(a4), respectively, with the corresponding cross-sectional views of the tungsten surface profiles depicted in Figs. 4(b1)–4(b4) and 5(b1)–5(b4); these are surface profiles along the black horizontal solid line marked in Figs. 4(a1) and 5(a1), respectively. The 3D views of the initial configuration and the final (meaning long-term, post-instability) configuration of the tungsten surface morphology corresponding to Figs. 4(a1), 4(a4), 5(a1), and 5(a4) are shown in Figs. 4(c), 4(d), 5(c), and 5(d), respectively. The evolution of the RMS surface roughness $SR(t)$ for the two cases of low-amplitude, long-wavelength perturbation from the planar surface of PFC tungsten shown in Figs. 4(e) and 5(e), respectively, indicates that the surface roughness increases only very slowly and gradually from the beginning of the simulations at steady-state He content in the nanobubble region due to the very low surface curvature gradient of the relatively flat surface (due to such a long perturbation wavelength); this stage of very slow evolution is followed by a very rapid increase in surface roughness as a result of the induced stress level in the nanobubble region becoming the dominant driving force for surface mass transport.

In Figs. 4(a4), 4(b4), 5(a4), and 5(b4), nanotendrils emanating from the PFC tungsten surface are clearly observed from the simulated morphological results of the surface at a sufficiently long time period of He plasma exposure and the average spacing between nanotendrils in both cases is 2.22 μm. In both cases, the evolution of the surface topography indicates that the nanotendrils form as a result of a tip-splitting instability of the original surface morphology, characterized by the long-wavelength perturbation, with the number of features (protrusions) generated by such tip splitting determining the number of nanotendrils that form and grow after the instability is triggered. Also, in both cases, the regular arrangement of the resulting nanotendrils on the surface is a result of the specified (deterministic, as opposed to random) and geometrically symmetric original perturbation from the planar PFC surface morphology. However, regardless of the detailed dynamics of the surface morphological

response, the resulting nanotendril arrangement on the surface is consistent with the predictions of linear stability theory (as indicated by the proximity of the resulting nanotendril spacing to the maximally unstable wavelength predicted by the linear stability theory).

To obtain a fundamental understanding for the dependence of the number of nanotendrils emanating from the surface of He plasma-exposed tungsten, we developed a weakly nonlinear tip-splitting instability theory, following the approach we developed in previous studies of surface morphological response of coherently strained epitaxial thin films [59,61–63]. In the present study, we monitor the surface morphological response of PFC tungsten upon disturbing according to a low-amplitude long-wavelength perturbation its planar surface morphology under the action of biaxial compressive stress originating from the over-pressurized helium bubbles in the near-surface (nanobubble) region at steady state of He concentration. Furthermore, to compute the onset of nanotendril formation on the PFC tungsten surface, we follow the approach of Ref. [50] to obtain all the subharmonics (higher-order terms with wave number $n\tilde{k}$) of the initial plane-wave perturbation (linear-order term with wave number $\tilde{k}$) in the solution for the surface height function of the evolving surface morphology. The growth of any such subharmonic will trigger a tip-splitting instability and cause the formation of multiple ripples per original wavelength of the surface perturbation. The growth rate of such subharmonic ripples with wave number $n\tilde{k}$ is expressed as

$$\tilde{\omega}^{(n)} = -(n\tilde{k})^4 + 2(n\tilde{k})^3 - \Xi_{\rm I}(n\tilde{k})^2 + 2\Xi_{\rm I}(n\tilde{k}). \quad (6)$$

The fastest growth rate $\tilde{\omega}^{(n)}$ among all the subharmonics of integer mode n with wave number $n\tilde{k}$ for $n \geqslant 1$ satisfies the relations

$$\tilde{\omega}^{(n-1)} \leqslant \tilde{\omega}^{(n)} \geqslant \tilde{\omega}^{(n+1)}, \quad (7)$$

yielding for the dominant mode n that controls the number of multiple ripples (surface features) on the resulting surface profiles (along a lateral direction)

$$[\zeta(n+1) + \xi(n+1)] - \frac{\phi(n+1)}{3} \leqslant \tilde{k} \leqslant [\zeta(n) + \xi(n)] - \frac{\phi(n)}{3}, \quad (8)$$

where

$$\zeta(n) = -\mathrm{sgn}(R(n))[|R(n)| + \sqrt{R(n)^2 - Q(n)^3}]^{1/3} \quad (9)$$

and

$$\xi(n) = Q(n)/\zeta(n). \quad (10)$$

The coefficients in Eqs. (9) and (10) are $Q(n) = \frac{\phi(n)^2 - 3\chi(n)}{9}$ and $R(n) = \frac{2\phi(n)^3 - 9\phi(n)\chi(n) + 27\psi(n)}{54}$, where $\phi(n) = \frac{-2[n^3-(n-1)^3]}{[n^4-(n-1)^4]}$, $\chi(n) = \frac{\Xi_{\rm I}[n^2-(n-1)^2]}{[n^4-(n-1)^4]}$, and $\psi(n) = \frac{-2\Xi_{\rm I}}{[n^4-(n-1)^4]}$.

Figure 6 shows a comparison between the number of 1D surface features N_f per original perturbation wavelength predicted from the weakly nonlinear tip-splitting instability theory (blue line segments) with the simulation results (red open circles) starting with a specific low-amplitude long-wavelength (λ_p) perturbation from a planar surface morphology under the specified He irradiation conditions. From this comparison, we conclude that the predictions for the post-instability morphology on the PFC tungsten surface from this stability analysis are in excellent qualitative agreement with the fully nonlinear simulation results spanning the full range of perturbation wavelengths examined in this study, including the results depicted in Figs. 4(a4), 4(b4), 5(a4), and 5(b4), $N_f = 9$ and $N_f = 5$, respectively. Our weakly nonlinear tip-splitting instability theory predicts that long-wavelength (low-k) surface perturbations can induce linearly unstable subharmonics, which govern the post-instability surface (pattern) morphology mediated by the tip-splitting mechanism. For example, as can be seen in Fig. 3, a surface perturbation with $\tilde{k} = 0.5$ will induce the unstable subharmonics of $2\tilde{k} = 1.0$ and $3\tilde{k} = 1.5$, and the one with wave number $3\tilde{k} = 1.5$ has the highest growth rate according to the linear stability theory; therefore, three secondary ripples are expected to form per original wavelength of the initial perturbation with $\tilde{k} = 0.5$ to cause PFC surface morphological instability and drive the surface morphological evolution. In brief, the weakly nonlinear tip-splitting instability theory provides a full interpretation on how long-wavelength perturbations will evolve to generate a surface morphology with nanotendrils arranged in space consistently with the key prediction of the linear stability theory, which also explains the post-instability pattern forming on the surface as a result of a random low-amplitude perturbation of its planar morphology.

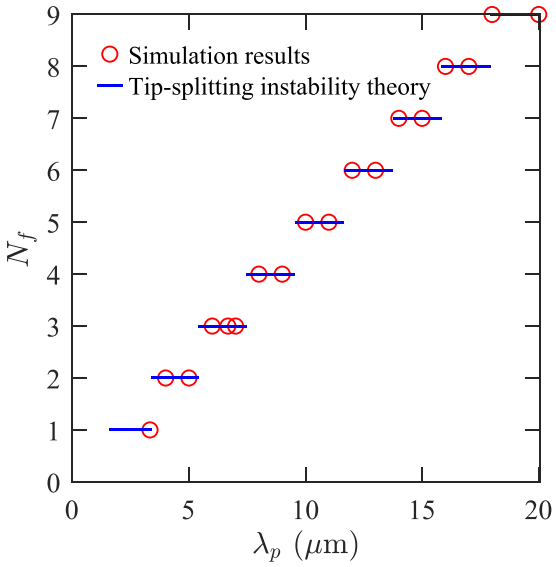

FIG. 6. Dependence of number of surface features in 1D surface profile, N_f, on the surface perturbation wavelength λ_p, following the surface morphological instability triggered on a PFC W(110) surface under conditions identical to those in Fig. 2 and simulation parameters identical to those in Figs. 4 and 5. The simulation results and the predictions of the weakly nonlinear tip-splitting instability theory are denoted by red open circles and blue solid line segments, respectively.

Figure 7(a) shows the evolution over the entire plasma exposure period of the surface roughness $\Delta(t)$ normalized by the initial surface roughness Δ_0 until the evolution has reached the "time-to-failure", t_f, which is determined by the asymptotes of the evolution curves: $\Delta(t)/\Delta_0 \to \infty$ as $t \to t_f$,

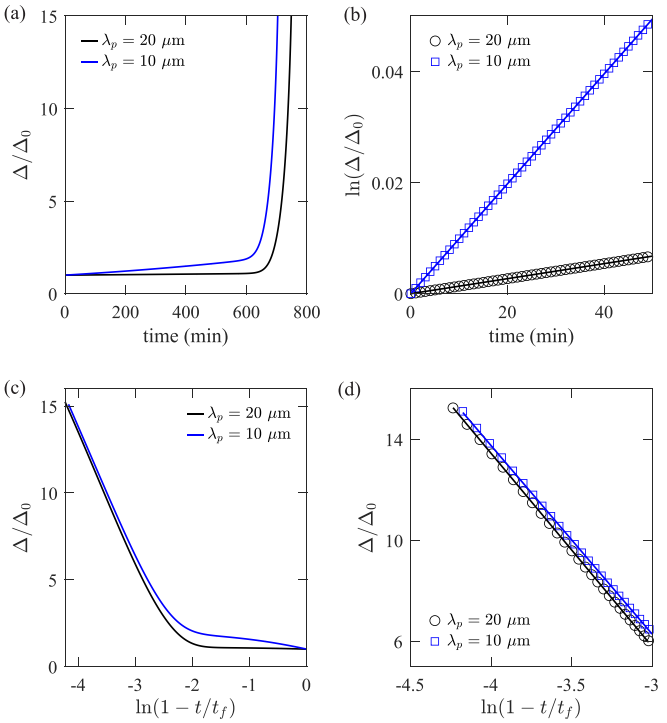

FIG. 7. (a) Evolution of the RMS surface roughness, denoted as $\Delta(t)$, under He plasma irradiation conditions identical to those in Fig. 2, with an initial surface roughness $\Delta_0 = 5$ nm. The solid black and solid blue lines correspond to simulation results starting with specific low-amplitude perturbations from the planar surface morphology identical to those in Figs. 4 and 5, respectively. (b) Exponential surface roughness evolution during the initial stage of growth of the low-amplitude, long-wavelength surface perturbation; the open symbols and solid lines represent simulation results and optimal linear fits (in a semilogarithmic plot) to the simulation predictions, respectively. [(c) and (d)] Evolution of the RMS surface roughness, $\Delta(t)$, for the two cases in (a) plotted as (c) a function of $\ln(1 - t/t_f)$ and (d) a function of $\ln(1 - t/t_f)$ at times t near the time to failure, t_f; the open symbols and solid lines represent simulation results and optimal linear fits to the simulation predictions, respectively.

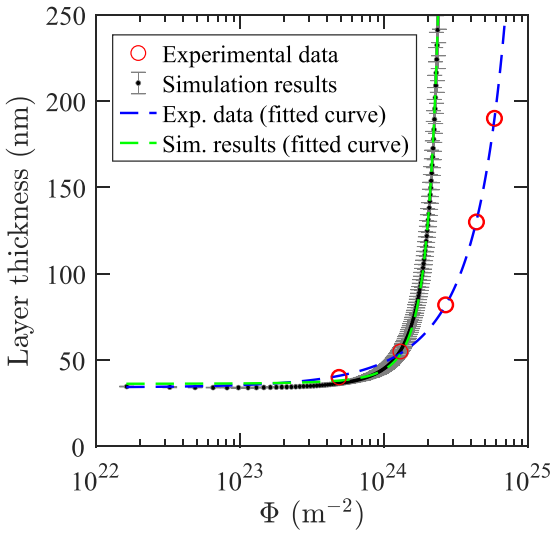

FIG. 8. Comparison of experimental data for fuzz layer thickness as a function of He fluence in plasma-exposed tungsten with simulation results for average nanotendril height evolution shifted upwards by h_0 under consistent plasma exposure conditions. Experimental data and simulation predictions are denoted by red open circles and small black solid circles, respectively, while optimal fitted curves to experimental measurements and model-predicted simulation results are denoted by blue and green dashed lines, respectively. In the simulations, the He plasma irradiation conditions are identical to those in Fig. 2. The error bars in the simulation results correspond to statistical errors from five independent simulations with different initial surface configurations of random low-amplitude perturbations from the planar surface morphology.

for the two representative cases of the initial long-wavelength perturbations on the planar He-irradiated tungsten surface at perturbation wavelengths $\lambda_p = 10$ μm (blue solid curve) and $\lambda_p = 20$ μm (black solid curve) corresponding to the cases of Figs. 5 and 4, respectively. In Fig. 7(b), we plot the natural logarithms of the normalized surface roughness evolution, $\ln(\Delta(t)/\Delta_0)$, for both λ_p values with the simulation results shown as blue open squares and black open circles, respectively, with the linear least-square fits to the simulation results shown as a blue solid curve and a black solid curve, respectively. The linear fits are excellent and confirm that the long-wavelength perturbations from the W(110) surface grow exponentially at the initial stage of the surface evolution. Figure 7(c) shows the normalized surface roughness evolution, $\Delta(t)/\Delta_0$, as a function of $\ln(1 - t/t_f)$ for both λ_p values at 10 μm (blue solid curve) and 20 μm (black solid curve). To observe clearly the long-term evolution trend of the normalized surface roughness, we plot $\Delta(t)/\Delta_0$ as a function of $\ln(1 - t/t_f)$ in the vicinity of the time-to-failure as shown in Fig. 7(d); the simulation results for both λ_p values are denoted by blue open squares and black open circles and the respective linear least-square fits are represented by the blue and black solid lines. The dynamic scaling relationship, $\Delta(t)/\Delta_0 \sim \ln(1 - t/t_f)$, that is established by the perfect linear fits of Fig. 7(d), implies that the long-term surface dynamics as t approaches t_f is governed by a logarithmic singularity.

C. Comparison of modeling results with experimental measurements of fuzz layer thickness on PFC tungsten

Figure 8 shows a comparison of our modeling predictions for PFC tungsten surface growth with experimental measurements of fuzz layer thickness evolution following the experimental procedures described in Sec. II C; small black solid circles and red open circles denote simulation results and experimental data, respectively, while dashed green and blue curves represent optimal fits to the simulation and experimental data, respectively, according to the exponential function $f(\Phi) = a\exp(b\Phi) + c$. In the above exponential functional form, the fluence Φ is the product of the imposed He flux on the PFC surface times t. The simulation predictions for the fuzz layer thickness correspond to the simulation results for the average nanotendril height shifted upwards by the nanobubble region thickness h_0 under the plasma exposure conditions used to produce the results in Fig. 2. It is evident

from Fig. 8 that the simulation results are in good agreement with the experimental data at the early stage of surface growth for He fluences up to $\sim 10^{24}$ m^{-2}. Specifically, at this early growth stage, the fitted exponential curves to the layer thickness evolution data from both simulation and experiment are in excellent agreement with each other and confirm that the fuzz layer thickness on the PFC tungsten surface undergoes exponential growth at the early stage of plasma exposure. However, the simulated layer thickness growth rate becomes much faster than the experimentally measured growth rate at He fluences higher than $\Phi \approx 2 \times 10^{24}$ m^{-2}. It should be mentioned that, at longer times, dynamic scaling of the simulation results shown in Fig. 8 demonstrates that the growing (nanotendril) layer diverges according to the logarithmic singularity highlighted in Fig. 7.

IV. DISCUSSION

Our numerical simulation results, in conjunction with our theoretical analyses of surface morphological stability based on our model of surface evolution for PFC tungsten exposed to He implantation, demonstrate that the onset of fuzz formation in He plasma-exposed tungsten is the outcome of a stress-induced surface morphological instability. The stress, in the form of equi-biaxial compressive stress in the near-surface PFC region, is developed due to the formation of over-pressurized He nanobubbles and plays a major role in the surface morphological response. Specifically, stress-induced surface diffusion overcomes the (smoothening) action of curvature-driven surface diffusion and triggers a morphological instability leading to a pattern of nanotendrils that emanate from the surface and keep growing under the action of the stress, while the role of subsurface defect dynamics approximated by a flux of self-interstitial atoms toward the surface after the He content in the near-surface region reaches steady state is not significant enough to affect the competition between the two driving forces of surface diffusion that determine the surface morphological evolution. Under typical low-energy He implantation conditions, the nanotendrils grow to reach heights of tens of nanometers at times over one hour of plasma exposure. The evolution of the PFC surface morphology is monitored from an initial configuration that consists of a low-amplitude perturbation of the planar PFC surface morphology after the He content in the near-surface nanobubble region reaches steady state (typically achieved within a few minutes). Regardless of the wavelength of the surface perturbation, which ranges in our study from the nanometer scale in random fluctuations from the planar surface state to tens of micrometers, a consistent post-instability pattern of nanotendrils forms on the surface characterized by an average nanotendril separation of 2–2.5 μm. The resulting post-instability surface topography is characterized in detail and explained fully by the predictions of linear stability theory and a weakly nonlinear tip-splitting instability theory.

Surface features on PFC tungsten with the heights predicted by our model after over one hour of plasma exposure and separation distances on the order of 1 μm have been observed experimentally on tungsten surfaces exposed to He plasmas [16]. However, in addition to these (nanotendril) features, which we can call coarse surface features, the experiments also reveal (within such coarse features) the appearance of finer surface features (nanotendrils) with widths and separation distances on the order of 100 nm. Such finer-scale nanotendrils have not been captured in this study and cannot be predicted by the surface evolution model implemented in this article. Nevertheless, we have recently demonstrated that fine surface features (nanotendrils) with average separation distances of $\sim$150 nm can be predicted on the PFC tungsten surface by augmenting the surface evolution model used in this study to incorporate a surface hole formation effect as a result of bubble bursting that, in addition to releasing He and maintaining the He content in the PFC near-surface region at steady state, also leads to formation of craters on the surface with dimensions on the order of 10 nm [38].

Our model predicts successfully the surface growth rates at the onset of fuzz formation, in agreement with the experimental data. However, the predicted surface growth rates are much faster than the experimental ones at longer times (higher He fluences) as the fuzz layer grows; this long-term overprediction of the surface growth rate by our model is attributed to the fast long-term dynamics of the surface morphological instability established without incorporating into the model additional subsurface bubble dynamical phenomena that significantly affect the long-term surface morphological response. However, the experimental results for the evolution of the fuzz layer thickness shown in Fig. 8 also provide a more detailed picture of the onset of the fuzz layer growth from the beginning of the PFC tungsten surface exposure to a He plasma reported in Ref. [9]. Our experiments, supported by our modeling predictions, and combined with the experimental results of Ref. [9] demonstrate that the growth of the fuzz layer on the PFC tungsten surface is a two-stage process, with a first stage (fuzz formation onset) where the growth rate is exponentially fast followed by a second stage where the growth rate is substantially reduced. The transition between the two stages of the fuzz layer growth process corresponds to the incubation fluence in the experimental literature.

V. SUMMARY AND CONCLUSIONS

In summary, we presented a systematic computational and theoretical analysis based on an atomistically informed and properly parameterized continuum-scale model of PFC tungsten surface morphological evolution that establishes the onset of fuzz formation in He plasma exposed surfaces as a surface morphological instability. This morphological response constitutes a stress-induced long-wavelength surface instability phenomenon driven by surface diffusional dynamics dominated by the stress generated in the PFC near-surface region as a result of the formation in this region of over-pressurized He bubbles from the He implantation into the PFC tungsten. The instability causes a low-amplitude disturbance of a PFC tungsten surface with planar morphology to evolve into a rough surface characterized by a pattern of nanotendrils that emanate from the surface and grow upon continued plasma exposure after the He content in the near-surface region reaches steady state. Independent of the geometrical features of the initial surface perturbation, random or regular at any perturbation wavelength, the key feature of the nanotendril pattern,

namely, the average separation distance between nanotendrils, is determined by the predictions of linear stability theory resulting in a nanotendril separation on the order of 1 μm, consistent with the separation of the coarse PFC tungsten surface features observed experimentally [16]. Long-wavelength perturbations evolve to such a nanotendril pattern according to a surface morphological response governed by a tip-splitting instability. At an early stage of plasma exposure, the resulting nanotendrils grow at a rate that is consistent with experimental measurements of fuzz layer growth, but the model overpredicts the surface growth rate at fluences above $\sim 10^{24}$ m^{-2}.

Although our PFC surface evolution model and morphological stability analysis based on the model provide a fundamental explanation for the onset of fuzz formation in PFC tungsten and valuable insights into the dynamics of the fuzz formation process, the current version of the model is missing important physics of subsurface bubble dynamical phenomena under He plasma exposure; these include new bubble formation in the nanobubble region, bubble coalescence, He bubble bursting and subsequent crater formation, as well as dislocation loop punching from large He bubbles. In order to fully capture the formation of fuzz-like surface nanostructure and nanotendril evolution in PFC tungsten, a modified representation of the PFC tungsten surface is required in conjunction with a much finer surface grid coupled with direct incorporation into our continuum-scale model of the above mentioned bubble dynamical phenomena in the near-surface region of PFC tungsten. In addition to the available atomistic information and numerical implementation improvements, these modeling and simulation developments require linking of our continuum-scale model with cluster-dynamics models of subsurface structural evolution in PFC tungsten. Such modeling and simulation efforts are currently underway, and the findings of these efforts will be presented in future publications.

The data that support the findings of this study are available from the corresponding author upon reasonable request.

ACKNOWLEDGMENTS

CSC and DM acknowledge support from the U.S. Department of Energy, Office of Fusion Energy Sciences (OFES) and Office of Advanced Scientific Computing Research through the Scientific Discovery through Advanced Computing (SciDAC) project on Plasma-Surface Interactions under Award No. DE-SC0018421. DD and BDW were supported by the U.S. Department of Energy, Office of Fusion Energy Sciences (OFES) and Office of Advanced Scientific Computing Research through the Scientific Discovery through Advanced Computing (SciDAC) project on Plasma-Surface Interactions under UT-Battelle Sub-contract 4000159718, and partially supported by OFES Award No. DE-SC0006661. RDK acknowledges funding support from the U.S. Department of Energy, Office of Fusion Energy Sciences, through the Fusion Materials program. Sandia National Laboratories is a multimission laboratory managed and operated by National Technology and Engineering Solutions of Sandia LLC, a wholly owned subsidiary of Honeywell International Inc. for the U.S. Department of Energy's National Nuclear Security Administration under Contract No. DE-NA0003525.

[1] J. W. Davis, V. R. Barabash, A. Makhankov, L. Plöchl, and K. T. Slattery, Assessment of tungsten for use in the ITER plasma facing components, J. Nucl. Mater. **258-263**, 308 (1998).

[2] H. Bolt, V. Barabash, W. Krauss, J. Linke, R. Neu, S. Suzuki, N. Yoshida, and ASDEX Upgrade Team, Materials for the plasma-facing components of fusion reactors, J. Nucl. Mater. **329-333**, 66 (2004).

[3] J. Roth, E. Tsitrone, T. Loarer, V. Philipps, S. Brezinsek, A. Loarte, G. F. Counsell, R. P. Doerner, K. Schmid, O. V. Ogorodnikova, and R. A. Causey, Tritium inventory in ITER plasma-facing materials and tritium removal procedures, Plasma Phys. Controlled Fusion **50**, 103001 (2008).

[4] G. J. van Rooij, J. W. Coenen, L. Aho-Mantila, S. Brezinsek, M. Clever, R. Dux, M. Groth, K. Krieger, S. Marsen, G. F. Matthews, A. Meigs, R. Neu, S. Potzel, T. Pütterich, J. Rapp, M. F. Stamp, the ASDEX Upgrade Team, and JET-EFDA Contributors, Tungsten divertor erosion in all metal devices: Lessons from the ITER like wall of JET, J. Nucl. Mater. **438**, S42 (2013).

[5] S. Takamura, N. Ohno, D. Nishijima, and S. Kajita, Formation of nanostructured tungsten with arborescent shape due to helium plasma irradiation, Plasma Fusion Res. **1**, 051 (2006).

[6] S. Kajita, W. Sakaguchi, N. Ohno, N. Yoshida, and T. Saeki, Formation process of tungsten nanostructure by the exposure to helium plasma under fusion relevant plasma conditions, Nucl. Fusion **49**, 095005 (2009).

[7] M. J. Baldwin, R. P. Doerner, D. Nishijima, K. Tokunaga, and Y. Ueda, The effects of high fluence mixed-species (deuterium, helium, beryllium) plasma interactions with tungsten, J. Nucl. Mater. **390-391**, 886 (2009).

[8] M. J. Baldwin, T. C. Lynch, R. P. Doerner, and J. H. Yu, Nanostructure formation on tungsten exposed to low-pressure rf helium plasmas: A study of ion energy threshold and early stage growth, J. Nucl. Mater. **415**, S104 (2011).

[9] T. J. Petty, M. J. Baldwin, M. I. Hasan, R. P. Doerner, and J. W. Bradley, Tungsten 'fuzz' growth re-examined: the dependence on ion fluence in non-erosive and erosive helium plasma, Nucl. Fusion **55**, 093033 (2015).

[10] K. Wang, R. P. Doerner, M. J. Baldwin, F. W. Meyer, M. E. Bannister, A. Darbal, R. Stroud, and C. M. Parish, Morphologies of tungsten nanotendrils grown under helium exposure, Sci. Rep. **7**, 42315 (2017).

[11] Q. Yang, Y.-W. You, L. Liu, H. Fan, W. Ni, D. Liu, C. S. Liu, G. Benstetter, and Y. Wang, Nanostructured fuzz growth on tungsten under low-energy and high-flux He irradiation, Sci. Rep. **5**, 10959 (2015).

[12] S. Kajita, S. Takamura, N. Ohno, D. Nishijima, H. Iwakiri, and N. Yoshida, Sub-ms laser pulse irradiation on tungsten target

damaged by exposure to helium plasma, Nucl. Fusion **47**, 1358 (2007).

[13] W. Sakaguchi, S. Kajita, N. Ohno, and M. Takagi, In situ reflectivity of tungsten mirrors under helium plasma exposure, J. Nucl. Mater. **390-391**, 1149 (2009).

[14] L. Hu, B. D. Wirth, and D. Maroudas, Thermal conductivity of tungsten: Effects of plasma-related structural defects from molecular-dynamics simulations, Appl. Phys. Lett. **111**, 081902 (2017).

[15] M. Seo, J. R. Echols, and A. L. Winfrey, Morphological and nanomechanical changes in tungsten in high heat flux conditions, npj Mater. Degrad. **4**, 30 (2020).

[16] D. Dasgupta, R. D. Kolasinski, R. W. Friddle, L. Du, D. Maroudas, and B. D. Wirth, On the origin of 'fuzz' formation in plasma-facing materials, Nucl. Fusion **59**, 086057 (2020).

[17] K. D. Hammond, Helium, hydrogen, and fuzz in plasma-facing materials, Mater. Res. Express **4**, 104002 (2017).

[18] K. D. Hammond, S. Blondel, L. Hu, D. Maroudas, and B. D. Wirth, Large-scale atomistic simulations of low-energy helium implantation into tungsten single crystals, Acta Mater. **144**, 561 (2018).

[19] K. D. Hammond, I. V. Naeger, W. Widanagamaachchi, L.-T. Lo, D. Maroudas, and B. D. Wirth, Helium flux effects on bubble growth and surface morphology in plasma-facing tungsten from large-scale molecular dynamics simulations, Nucl. Fusion **59**, 066035 (2019); K. D. Hammond, B. F. Lee, I. V. Naeger, W. Widanagamaachchi, L.-T. Lo, D. Maroudas, and B. D. Wirth, Corrigendum and Addendum: Helium flux effects on bubble growth and surface morphology in plasma-facing tungsten from large-scale molecular dynamics simulations (2019 Nucl. Fusion 59 066035), *ibid.* **60**, 129401 (2020).

[20] F. Sefta, N. Juslin, K. D. Hammond, and B. D. Wirth, Molecular dynamics simulations on the effect of subsurface helium bubbles on the sputtering yield of tungsten, J. Nucl. Mater. **438**, S493 (2013).

[21] S. Blondel, D. E. Bernholdt, K. D. Hammond, and B. D. Wirth, Continuum-scale modeling of helium bubble bursting under plasma-exposed tungsten surfaces, Nucl. Fusion **58**, 126034 (2018); Corrigendum: Continuum-scale modeling of helium bubble bursting under plasma-exposed tungsten surfaces (2018 Nucl. Fusion 58 126034), **59**, 029501 (2019).

[22] F. Sefta, K. D. Hammond, N. Juslin, and B. D. Wirth, Tungsten surface evolution by helium bubble nucleation, growth and rupture, Nucl. Fusion **53**, 073015 (2013).

[23] F. Sefta, N. Juslin, and B. D. Wirth, Helium bubble bursting in tungsten, J. Appl. Phys. **114**, 243518 (2013).

[24] M. S. Abd El Keriem, D. P. van der Werf, and F. Pleiter, Trap mutation in He-doped ion-implanted tungsten, Hyperfine Interact. **79**, 787 (1993).

[25] L. Sandoval, D. Perez, B. P. Uberuaga, and A. F. Voter, Competing Kinetics and He Bubble Morphology in W, Phys. Rev. Lett. **114**, 105502 (2015).

[26] A. Weerasinghe, B. D. Wirth, and D. Maroudas, Elastic properties of plasma-exposed tungsten predicted by molecular-dynamics simulations, ACS Appl. Mater. Interfaces **12**, 22287 (2020).

[27] S. I. Krasheninnikov, Viscoelastic model of tungsten 'fuzz' growth, Phys. Scr. **T145**, 014040 (2011).

[28] Y. V. Martynenko and M. Y. Nagel, Model of fuzz formation on a tungsten surface, Plasma Phys. Rep. **38**, 996 (2012).

[29] A. Lasa, S. K. Tähtinen, and K. Nordlund, Loop punching and bubble rupture causing surface roughening—A model for W fuzz growth, Europhys. Lett. **105**, 25002 (2014).

[30] P. Fiflis, D. Curreli, and D. N. Ruzic, Direct time-resolved observation of tungsten nanostructured growth due to helium plasma exposure, Nucl. Fusion **55**, 033020 (2015).

[31] A. M. Ito, A. Takayama, Y. Oda, T. Tamura, R. Kobayashi, T. Hattori, S. Ogata, N. Ohno, S. Kajita, M. Yajima, Y. Noiri, Y. Yoshimoto, S. Saito, S. Takamura, T. Murashima, M. Miyamoto, and H. Nakamura, Hybrid simulation research on formation mechanism of tungsten nanostructure induced by helium plasma irradiation, J. Nucl. Mater. **463**, 109 (2015).

[32] A. M. Ito, A. Takayama, Y. Oda, T. Tamura, R. Kobayashi, T. Hattori, S. Ogata, N. Ohno, S. Kajita, M. Yajima, Y. Noiri, Y. Yoshimoto, S. Saito, S. Takamura, T. Murashima, M. Miyamoto, and H. Nakamura, Molecular dynamics and Monte Carlo hybrid simulation for fuzzy tungsten nanostructure formation, Nucl. Fusion **55**, 073013 (2015).

[33] G. Valles, I. Martin-Bragado, K. Nordlund, A. Lasa, C. Björkas, E. Safi, J. M. Perlado, and A. Rivera, Temperature dependence of underdense nanostructure formation in tungsten under helium irradiation, J. Nucl. Mater. **490**, 108 (2017).

[34] A. M. Ito, A. Takayama, and H. Nakamura, Triple hybrid simulation method for tungsten fuzzy nanostructure formation, Plasma Fusion Res. **13**, 3403061 (2018).

[35] S. Kajita, N. Yoshida, N. Ohno, and Y. Tsuji, Growth of multifractal tungsten nanostructure by He bubble induced directional swelling, New J. Phys. **17**, 043038 (2015).

[36] D. Dasgupta, D. Maroudas, and B. D. Wirth, Prediction of temperature range for the onset of fuzz formation in helium-plasma-implanted tungsten, Surf. Sci. **698**, 121614 (2020).

[37] C.-S. Chen, D. Dasgupta, A. Weerasinghe, B. D. Wirth, and D. Maroudas, Effects of elastic softening and helium accumulation kinetics on surface morphological evolution of plasma-facing tungsten, Nucl. Fusion **61**, 016016 (2021).

[38] C.-S. Chen, D. Dasgupta, B. D. Wirth, and D. Maroudas, Hole formation effect on surface morphological response of plasma-facing tungsten, J. Appl. Phys. **129**, 193302 (2021).

[39] K. B. Woller, D. G. Whyte, and G. M. Wright, Dynamic measurement of the helium concentration of evolving tungsten nanostructures using Elastic Recoil Detection during plasma exposure, J. Nucl. Mater. **463**, 289 (2015).

[40] F. Hofmann, D. Nguyen-Manh, M. R. Gilbert, C. E. Beck, J. K. Eliason, A. A. Maznev, W. Liu, D. E. J. Armstrong, K. A. Nelson, and S. L. Dudarev, Lattice swelling and modulus change in a helium-implanted tungsten alloy: X-ray micro-diffraction, surface acoustic wave measurements, and multiscale modelling, Acta Mater. **89**, 352 (2015).

[41] R. J. Asaro and W. A. Tiller, Interface morphology development during stress corrosion cracking: Part I. Via surface diffusion, Metall. Mater. Trans. B **3**, 1789 (1972).

[42] M. A. Grinfeld, The stress driven instability in elastic crystals: Mathematical models and physical manifestations, J. Nonlinear Sci. **3**, 35 (1993).

[43] R. H. Torii and S. Balibar, Helium crystals under stress: The Grinfeld instability, J. Low Temp. Phys. **89**, 391 (1992).

[44] J. Berréhar, C. Caroli, C. Lapersonne-Meyer, and M. Schott, Surface patterns on single-crystal films under uniaxial stress: Experimental evidence for the Grinfeld instability, Phys. Rev. B **46**, 13487 (1992).

[45] V. V. Tsukruk and D. H. Reneker, Periodic surface instabilities in stressed polymer solids, Phys. Rev. B **51**, 6089 (1995).
[46] L. Thilly, J. Colin, F. Lecouturier, J. P. Peyrade, J. Grilhé, and S. Askénazy, Interface instability in the drawing process of copper/tantalum conductors, Acta Mater. **47**, 853 (1999).
[47] Y. Pang and R. Huang, Nonlinear effect of stress and wetting on surface evolution of epitaxial thin films, Phys. Rev. B **74**, 075413 (2006).
[48] D. J. Srolovitz, On the stability of surfaces of stressed solids, Acta Metall. **37**, 621 (1989).
[49] Y. Xiang and W. E, Nonlinear evolution equation for the stress-driven morphological instability, J. Appl. Phys. **91**, 9414 (2002).
[50] L. Du, D. Dasgupta, and D. Maroudas, Weakly nonlinear theory of secondary rippling instability in surfaces of stressed solids, J. Appl. Phys. **118**, 035303 (2015).
[51] V. Tomar, M. R. Gungor, and D. Maroudas, Current-Induced Stabilization of Surface Morphology in Stressed Solids, Phys. Rev. Lett. **100**, 036106 (2008).
[52] V. Tomar, M. R. Gungor, and D. Maroudas, Current-induced stabilization of surface morphology in stressed solids: Validation of linear stability theory, J. Appl. Phys. **107**, 103525 (2010).
[53] G. Antczak and G. Ehrlich, Long Jump Rates in Surface Diffusion: W on W(110), Phys. Rev. Lett. **92**, 166105 (2004).
[54] T. Faney and B. D. Wirth, Spatially dependent cluster dynamics modeling of microstructure evolution in low energy helium irradiated tungsten, Modell. Simul. Mater. Sci. Eng. **22**, 065010 (2014).
[55] See Supplemental Material at http://link.aps.org/supplemental/10.1103/PhysRevMaterials.5.113403 for a detailed derivation of the linearized model for the surface morphological response of PFC tungsten, including a full description of the chemical potential of surface atoms and an asymptotic calculation of the elastic strain energy density in the near-surface region of PFC tungsten, as well as detailed focused ion beam (FIB) characterization of the helium-induced nanostructure layer in the near-surface region of PFC tungsten.
[56] S. E. Donnelly, The density and pressure of helium in bubbles in implanted metals: A critical review, Radiat. Eff. **90**, 1 (1985).
[57] K. D. Hammond, D. Maroudas, and B. D. Wirth, Theoretical model of helium bubble growth and density in plasma-facing metals, Sci. Rep. **10**, 2192 (2020).
[58] G. Tegze, G. Bansel, G. I. Tóth, T. Pusztai, Z. Fan, and L. Gránásy, Advanced operator splitting-based semi-implicit spectral method to solve the binary phase-field crystal equations with variable coefficients, J. Comput. Phys. **228**, 1612 (2009).
[59] L. Du and D. Maroudas, Theory of multiple quantum dot formation in strained-layer heteroepitaxy, Appl. Phys. Lett. **109**, 023103 (2016).
[60] C.-S. Wong, J. A. Whaley, T. Wada, S. Harayama, Y. Oya, and R. D. Kolasinski, Changes in surface morphology of helium-induced tungsten nanostructure during high-temperature annealing, Nucl. Mater. Energy **22**, 100730 (2020).
[61] A. Kumar, C.-S. Chen, and D. Maroudas, Fabrication of ordered arrays of quantum dot molecules based on the design of pyramidal pit patterns on semiconductor surfaces, Ind. Eng. Chem. Res. **59**, 2536 (2020).
[62] C.-S. Chen, A. Kumar, and D. Maroudas, On the formation of multiple quantum dots inside elongated pits on semiconductor films deposited epitaxially on pit-patterned substrates, Mater. Res. Express **6**, 086328 (2019).
[63] L. Du, M. Khenner, and D. Maroudas, Kinetics of nanoring formation on surfaces of stressed thin films, Phys. Rev. Materials **2**, 083403 (2018).